Topological Bands and Triply Degenerate Points in Non-Hermitian Hyperbolic Metamaterials

Junpeng Hou,[1] Zhitong Li,[2] Xi-Wang Luo,[1,*] Qing Gu,[2] and Chuanwei Zhang[1,†]
[1]Department of Physics, The University of Texas at Dallas, Richardson, Texas 75080-3021, USA
[2]Department of Electrical and Computer Engineering, The University of Texas at Dallas, Richardson, Texas 75080-3021, USA

(Received 31 August 2018; accepted 4 February 2020; published 21 February 2020)

Hyperbolic metamaterials (HMMs), an unusual class of electromagnetic metamaterials, have found important applications in various fields due to their distinctive properties. A surprising feature of HMMs is that even continuous HMMs can possess topological edge modes. However, previous studies based on equal-frequency surface (analogy of Fermi surface) may not correctly capture the topology of entire bands. Here we develop a topological band description for continuous HMMs that can be described by a non-Hermitian Hamiltonian formulated from Maxwell's equations. We find two types of three-dimensional non-Hermitian triply degenerate points with complex linear dispersions and topological charges ± 2 and 0 induced by chiral and gyromagnetic effects. Because of the photonic nature, the vacuum band plays an important role for topological edge states and bulk-edge correspondence in HMMs. The topological band results are numerically confirmed by direct simulation of Maxwell's equations. Our work presents a general non-Hermitian topological band treatment of continuous HMMs, paving the way for exploring interesting topological phases in photonic continua and device implementations of topological HMMs.

DOI: 10.1103/PhysRevLett.124.073603

Introduction.—Hyperbolic metamaterials (HMMs), also known as indefinite media, are a class of optical metamaterials with extreme anisotropy [1]: the effective permittivity (or permeability) tensor components that are parallel and perpendicular to the optical axis have opposite signs, therefore their optical properties resemble dielectric and metal in orthogonal directions [1,2]. Due to such unique property and associated indefinite dispersion, HMMs possess an infinite optical density of states, giving rise to applications in versatile fields [3–10] such as super-resolution microscopy, biosensing, lasing, etc.

Recently, it was proposed [11–13] that HMMs can serve as an ideal candidate for studying topological photonics in materials with continuous translational symmetry (i.e., no periodic lattice structure at optical wavelength scale or the periodicity goes to infinity) [14]. Topological photonics, the application of topological band theory in photonic systems, have generated great excitements for both fundamental studies and practical applications. Most studies have focused on periodic dielectric systems [15] (e.g., photonic crystals, coupled waveguides, and cavities), which are well described by band topology in Bloch basis based on the analogy between electromagnetic wave equations and Schrödinger's equation [16–28].

Different from Hermitian dielectric systems [18,19,29] with real-valued band structures, HMMs represent a continuous non-Hermitian system with complex eigenvalues due to their metal nature along one or two of the optical axes. Therefore two important questions naturally arise. Can a theory be developed for characterizing topological bands of such continuous non-Hermitian HMMs? If so, what new physics can arise from such topological band theory? We note that previous studies have introduced the equal frequency surface (EFS) to characterize the topology of HMMs [11–13] with photonic EFS corresponding to the Fermi surface in electronic materials. While the Fermi surface does contain certain information, the complete topological properties are encoded in the entire bands. As a result, the EFS theory is incomplete for investigating the topological properties of continuous non-Hermitian HMMs, and may lead to ambiguous (sometimes misleading or incorrect) predictions (see the Supplemental Material [30] for an example).

In this Letter, we answer these two important questions by developing a topological band description, along with the bulk-edge correspondence, for continuous HMMs. Our main results are as follows: (i) an effective non-Hermitian Hamiltonian for HMMs is derived from Maxwell's equations. Symmetry analysis shows the physics can be described by three bands (i.e., a spin-1 system). A proper gyromagnetic or chiral field opens a band gap between the upper and the other two bands except at $\mathbf{k} = 0$, which is a non-Hermitian triply degenerate point (TDP) [31–33] with complex linear band dispersions (i.e., a topological semimetal). The complex bulk spectrum exhibits an exceptional cone with the TDP as cone vertex. TDPs were studied recently in solid state [31,32] and ultracold atomic systems [33], but have not been explored in photonic materials or any non-Hermitian systems, and their real linear dispersions are very different from non-Hermitian TDPs.

The topological charge of the TDP at $\mathbf{k} = 0$ is ± 2 (0) for chiral (gyromagnetic) effect. For any fixed nonzero k_z, the HMM is a 2D Chern insulator, and the TDP emerges as the band gap closing point at $k_z = 0$. (ii) There exist surface states connecting the single TDP to infinity for both cases (change ± 2 or charge 0), which are illustrated through topological edge states in both 3D and 2D Chern insulators with fixed k_z using the bulk-edge correspondence. More importantly, the topological edge states can only be found in the common band gap of the HMMs and vacuum because, unlike electrons in solid-state materials, photons can propagate in the vacuum, forming vacuum band structures outside the HMMs. The edge states are purely real and do not suffer loss as the complex bulk, which, combining with the unique properties of HMMs, enable the design of novel optical devices such as topological lasing. And (iii) our theoretical predictions on topological bands and chiral edge states of HMMs are confirmed by numerically solving the Maxwell's equations using COMSOL simulations.

Non-Hermitian Hamiltonian and topological invariant.—The HMMs can be described by the source-free Maxwell's equations with the following constitutive relation

$$\boldsymbol{D} = \epsilon \boldsymbol{E} + i\gamma \boldsymbol{H}, \qquad \boldsymbol{B} = \mu \boldsymbol{H} - i\gamma \boldsymbol{E}, \tag{1}$$

based on the symmetrized Condon set [34], where ϵ, μ, and γ are 3×3 permittivity, permeability, and chirality tensors. Without gain and loss, they satisfy $\mu^\dagger = \mu$ and $\epsilon^\dagger = \epsilon$. The chirality term can be written as $\gamma = \mathrm{Tr}(\gamma) I/3 + N$ with I the identity matrix and N a real-valued symmetric trace-free tensor. The chiral and gyromagnetic effects for HMMs can be induced by nonzero γ and imaginary nondiagonal terms in ϵ or μ, respectively. The Maxwell's equations can be recast to a linear-transformation form $H|\Psi\rangle = \omega|\Psi\rangle$, with

$$H = \begin{pmatrix} \epsilon & i\gamma \\ -i\gamma & \mu \end{pmatrix}^{-1} \begin{pmatrix} 0 & p \\ -p & 0 \end{pmatrix}, \qquad |\Psi\rangle = \begin{pmatrix} \boldsymbol{E} \\ \boldsymbol{H} \end{pmatrix}, \tag{2}$$

where $p_{[mn]} = \varepsilon_{mnl}\nabla_l$ is an antisymmetric tensor operator ($p^T = -p$) defined through the Levi-Civita symbol ε_{mnl}. In the limit $\gamma \to 0$, Eq. (2) reduces to the Hermitian formalism in previous works [18,19,29] if ϵ and μ are positive-definite. In the context of HMMs, the Hamiltonian in Eq. (2) is generally non-Hermitian and possesses complex eigenvalues, therefore the topological classifications for Hermitian systems [35–37] do not apply.

The Hamiltonian has six bands, which appear in pairs $(\omega, -\omega)$ due to the symmetry $\Pi H \Pi^{-1} = -H$, where the symmetry operator Π is defined as the composite of chiral symmetry $\mathcal{C}$ and the operation $\gamma \to -\gamma$. Here $\mathcal{C} = \sigma_z \otimes I_3$ and σ_i represents a Pauli matrix in the $(\boldsymbol{E}, \boldsymbol{H})$ space. In addition, the state at $(\mathbf{k}, \omega)$ represents the same physical state as that at $(-\mathbf{k}, -\omega)$ due to the symmetry $H(-p) = -H(p)$, which holds for arbitrary H. When combined together, these symmetries dictate that only three bands are independent. Here we consider three bands with $\Re(\omega) \geq 0$ ($\Re$ takes the real part), which form an effective spin-1 system. Note that one band is a zero-energy ($\omega = 0$) flat band, which represents the static solutions $\boldsymbol{E} = \nabla d(\boldsymbol{r})$ and $\boldsymbol{H} = \nabla b(\boldsymbol{r})$. Interestingly, the three bands are always (triply) degenerate at $(\mathbf{k}, \omega) = 0$ for arbitrary H, independent of ϵ, μ, and γ.

The energy spectra for a non-Hermitian Hamiltonian are generally complex, and the topological invariants can be defined by either eigenvalues or eigenstates. The eigenvalue-based winding number for a closed loop in momentum space is defined as [38,39] $C_\omega = \oint d\mathbf{k}(\partial/\partial_{\mathbf{k}}) \arg[\omega(\mathbf{k})]$, which is generally trivial and irrelevant to the topological edge modes for HMMs discussed here. On the other hand, the bands for HMMs are separable in the complex plane, therefore the winding number $W = (1/\pi) \oint_{\mathcal{S}^1} d\mathbf{k} \cdot \mathcal{A}(\mathbf{k})$ and the Chern number $C = (1/2\pi) \oint_{\mathcal{S}} d\mathbf{S} \cdot \mathcal{F}$ based on eigenstates are well defined and quantized, which can be used to characterize the topological properties of HMMs. Here $\mathcal{S}^1$ is a closed 1D loop and $\mathcal{S}$ can be a closed 2D sphere $\mathcal{S}^2$ (or infinite plane $\mathcal{R}^2$) in the momentum space, $\mathcal{A}(\mathbf{k}) = -i_L \langle \Psi(\mathbf{k}) | \nabla_{\mathbf{k}} | \Psi(\mathbf{k}) \rangle_R$ and $\mathcal{F} = \nabla \times \mathcal{A}(\mathbf{k})$ are the Berry connection and Berry curvature, respectively, and $|\Psi(\mathbf{k})\rangle_R$ ($|\Psi(\mathbf{k})\rangle_L$) is the right (left) eigenstate [39] of the Hamiltonian. Among the three bands, the zero-energy flat band is topologically trivial, while the other two nonzero bands possess opposite topological invariants. Hereafter we only plot the two nonzero-energy bands with $\Re(\omega) > 0$ for better visualization.

Charge ± 2 TDPs from chiral effects.—Without chiral and gyromagnetic terms and assume $\epsilon = \mathrm{diag}(\epsilon_x > 0, \epsilon_y > 0, \epsilon_z < 0)$ and $\mu = I$ for hyperbolic dispersion, there is one degenerate line along the k_z axis between the two upper nonzero bands with $\epsilon_x = \epsilon_y$, as shown in Fig. 1(a). The degenerate line possesses a nontrivial winding number (defined by the highest band) $W = 2$ for a closed loop encircling the line [30]. The corresponding band structure in the $k_x - k_y$ plane with a fixed nonzero k_z contains a quadratic band touching point with winding number $W = 2$ at $(k_x, k_y) = (0, 0)$, which is computed on a closed circle enclosing the degenerate point. The band structures for $\epsilon_x \neq \epsilon_y$ are presented in the Supplemental Material [30].

The degeneracy between two nonzero bands along the k_z axis (except at $\mathbf{k} = 0$) can be lifted by breaking inversion symmetry using a chiral term [Fig. 1(b) with $\gamma = \mathrm{diag}(1, 0, 0)$]. For a fixed $k_z \neq 0$, the gap at the quadratic band touching point is opened, yielding 2D Chern insulators with opposite Chern numbers -1 and $+1$ for $k_z < 0$ and $k_z > 0$ because the inversion symmetry along the z axis is broken [Fig. 1(c)]. Note here that the 2D Chern number is always defined by the upper band that is fully gapped except at $\mathbf{k} = 0$. The 2D Chern number is integrated over the 2D infinite plane $\mathcal{R}^2$ in momentum space at a constant k_z and is quantized in continuous limit (see the Supplemental Material [30] for a proof). The lower nonzero band transits from real to imaginary eigenenergies along an

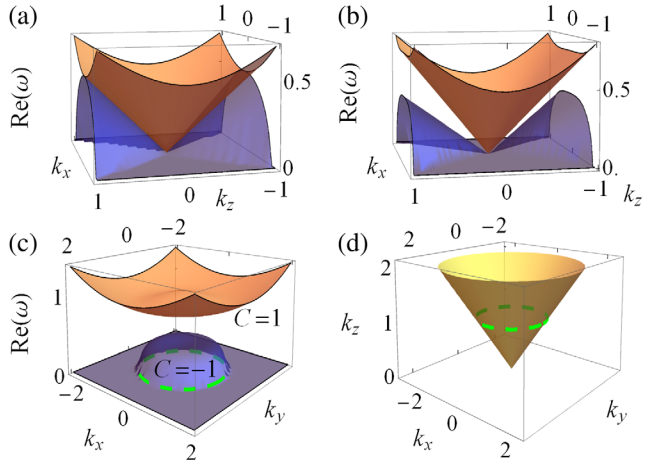

FIG. 1. Typical band structures for HMMs. (a) A HMM with $(\epsilon_x, \epsilon_y, \epsilon_z) = (4, 4, -3)$ exhibits a degenerate line along k_z axis between two nonzero bands. (b) The degenerate line (except $\mathbf{k} = 0$) in (a) is lifted by $\gamma = \mathrm{diag}(1, 0, 0)$. (c) Corresponding gapped topological bands in 2D $k_x - k_y$ plane for $k_z = 1$. See the Supplemental Material [30] for the imaginary bands. The dashed green circle is the exceptional ring. (d) The 3D exceptional cone in momentum space at $k_z \geq 0$.

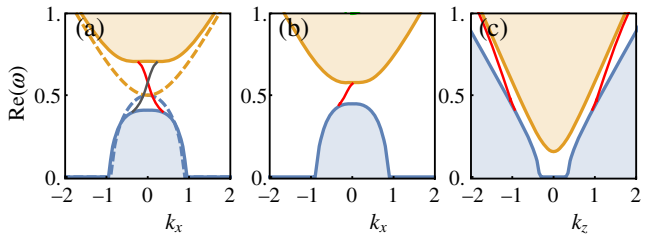

FIG. 2. 2D band structure with edge states. We choose $(\epsilon_x, \epsilon_y, \epsilon_z) = (4, 4, -3)$. The color-coded areas represent subbands under projection and solid red (or dark gray) curves are chiral surface waves with velocity $d\omega/dk$. (a) The edge states are induced by a pure chiral effect $\gamma = \mathrm{diag}(1, 0, 0)$ such that they possess opposite chirality for $k_z = +1$ (red) and $k_z = -1$ (dark gray) while the band structure remains the same. The two dashed curves show the bands with $\gamma = 0$. (b) The chiral edge states are the same at $k_z = \pm 1$ for a gyromagnetic term $\epsilon_{xy} = -\epsilon_{yx} = i$. (c) Same as (b) but we set $k_x = -0.3$ and compute the edge states along k_z. Here a zero charge TDP yields two edge states with opposite chirality.

exceptional ring with coalesced eigenstates [the green circle in Fig. 1(c)]. Such an exceptional ring at finite k_z shrinks to a point at $\mathbf{k} = 0$, resulting in a 3D *exceptional cone* with the cone vertex at $\mathbf{k} = 0$ [Fig. 1(d)].

The origin $\mathbf{k} = 0$ is a TDP with linear band dispersions [Fig. 1(b) and [30]], which, for the lower band, can appear in either real or imaginary spectrum along different momentum directions. Such a non-Hermitian TDP is quite different from the real TDPs in electronic and cold atomic Hermitian systems [31–33]. At $k_z = 0$, the band gaps for 2D Chern insulators close, yielding a topological charge $C = +2$ of the TDP that is equivalent to the change of 2D Chern number across $k_z = 0$. Here the topological charge is evaluated on a closed surface $\mathcal{S}^2$ enclosing $\mathbf{k} = 0$. Because there is only one charge $+2$ TDP in the HMM due to its continuous translational symmetry, there should be surface states connecting the TDP to infinity. We consider an open boundary condition along the y direction with a semi-infinite HMM in $y < 0$ and the vacuum (i.e., $\mu_v = \epsilon_v = I$) at $y > 0$, and the surface state is solved as Dyakonov wave [40]. Within the scope of this work, we find that the surface wave only has real energy despite the complex bulk spectrum. The obtained surface states in the k_x-k_z plane connect two bulk bands and vanish at the TDP. Because the band gap appears at different ω regions for different k_z, the commonly used surface spectral density at a fixed ω is not good for describing the surface states of continuous HMMs. For a fixed $k_z \neq 0$, the chiral edge states propagate along opposite directions (i.e., opposite velocities $d\omega/dk_x$) for $k_z > 0$ and $k_z < 0$ [Fig. 2(a)] because of their opposite bulk Chern numbers of 2D insulators. Although the lower band is purely imaginary in part of the momentum space, the edge states only connect to purely real parts.

Charge 0 TDP from gyromagnetic effects.—The degenerate line in Fig. 1(a) can also be gapped out by the gyromagnetic effect, leading to another type of TDP at $\mathbf{k} = 0$. We consider the gyromagnetic effect that is induced by a magnetic field along the z direction, which yields a pure imaginary nondiagonal term ϵ_{xy} ($\epsilon_{yx} = -\epsilon_{xy}$ to keep ϵ Hermitian). The resulting band structure is similar as Fig. 1(b) [see also Fig. 3(b). However, the Chern numbers for 2D bands in the k_x-k_y plane are $+1$ for both $k_z > 0$ and $k_z < 0$ because the magnetic field along the z direction, although it breaks the time-reversal symmetry, still preserves the inversion symmetry along the z axis. The Chern number changes sign with the sign of ϵ_{xy}, i.e., $\mathrm{sign}[\Im(\epsilon_{xy})]$ ($\Im$ takes the imaginary part). Although the band topology does not change across $k_z = 0$, the band gap still closes, leading a topological TDP at $\mathbf{k} = 0$ with charge 0 due to opposite Berry flux for $k_z > (<) 0$ [30].

Because of the same topology, the edge states for $k_z > 0$ and $k_z < 0$ propagate along the same direction [Figs. 2(b) and 3(b)]. We see for a given k_x and ω at the edge, there could be two surface states with opposite k_z. In Fig. 2(c), we show these two edge modes along k_z for a fixed k_x, which start from the lower band and gradually approach the upper band. As a comparison, there may be only one edge mode along k_z for a fixed large k_x with the chiral effect [30]. Such double edge modes originate from topologically trivial 2D bands in the k_y-k_z plane for a fixed k_x, which gives zero or even numbers of edge modes with opposite chirality.

We remark that when both gyromagnetic and chiral effects are considered, their competition would drive a transition between charge-2 and charge-0 TDPs. An example is shown explicitly in the Supplemental Material [30].

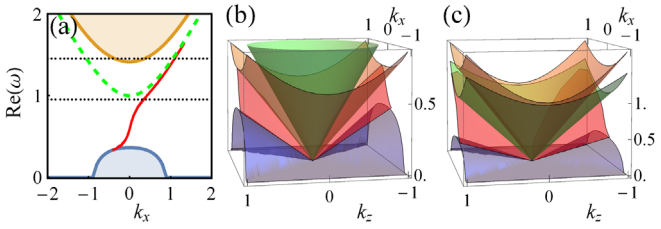

FIG. 3. (a) 2D band structure and edge states with a gyromagnetic term $\epsilon_{xy} = 3.5i$ for $k_z = 1$. The dashed green curve is the vacuum band, which is twofold degenerate. Two dashed curves (from top to bottom) give the frequencies of the line source in COMSOL simulations shown in Figs. 4(c) and 4(a). (b),(c) 3D band structures with edge states for $\epsilon_{xy} = 2i$ and $\epsilon_{xy} = 3.5i$, respectively. The red surfaces represent chiral surface waves and the green one is the vacuum band.

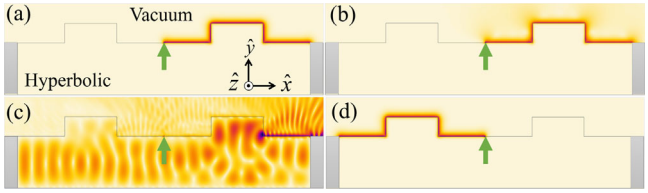

FIG. 4. COMSOL simulation results for our model, where a HMM is placed in vacuum with two absorption materials on two sides (gray-coded areas). The color represents the distribution of total electric field strength. The green arrow indicates the position of a line source, which is a plane wave along vertical direction, with input energy ω_I. The field propagates along the z direction. We choose the same parameters as those in Fig. 3(a) and tune the input source to (a) $\omega_I = 0.95$, (b) $\omega_I = 1$, and (c) $\omega_I = 1.45$. (d) Same as panel (a) except that the sign of the applied gyromagnetic term is opposite such that the chirality of the edge state is reversed.

Bulk-edge correspondence with vacuum bands.—Unlike electronic materials, a vacuum is not an insulator for photons and there exist photonic bands for a vacuum (although topologically trivial), i.e., the free space continuum. Because of its direct contact with the edges of HMMs, vacuum effects should be taken into account for edge states and bulk-edge correspondence. Here we illustrate the vacuum effects using gyromagnetic effects. For a small ϵ_{xy} term, the vacuum band is higher than both bulk bands of the HMM [the vacuum band was not shown in Figs. 2(b) and 2(c) for this reason]. With increasing $|\epsilon_{xy}|$, the band gap between the two nonzero bulk bands increases and the upper band would surpass the vacuum bands at a certain value of $|\epsilon_{xy}|$, after which the edge mode connects to the vacuum band, instead of the upper band, as shown in Fig. 3(a). This is because photons cannot localize at the boundary of the HMM after they diffuse into a vacuum. Since the vacuum band is topologically trivial, the physical properties of the surface waves like chirality are preserved.

In Figs. 3(b) and 3(c), we plot the 3D band structures with edge modes for both weak ($\epsilon_{xy} = 2i$) and strong ($\epsilon_{xy} = 3.5i$) gyromagnetic effects in the k_z-k_x plane, which show similar features as Figs. 2(b) and 3(a). Note that the vacuum band crosses $(\mathbf{k}, \omega) = 0$ and does not intersect with the nonzero upper HMM band away from the TDP because both bands increase linearly with respect to $|k|$. The surface states, starting from the TDP, always fill the common gap between the lower HMM band and either the upper HMM or vacuum bands, depending on which has the lower energy. For a given ϵ_{xy}, only one band [upper HMM band, Fig. 3(b), or vacuum band, Fig. 3(c), for weak and strong gyromagnetic effects, respectively] is connected by the surface states.

Numerical simulations.—The above topological band properties and corresponding edge states in continuous HMMs can be further confirmed through COMSOL mutiphysics. Here we choose three different values of line source frequency $\omega_I = 0.9$, 1 and 1.45, which correspond to band energies below the vacuum band, overlapping with the vacuum band, and overlapping with both the vacuum and bulk bands, respectively [Fig. 3(a)]. The simulation results are shown in Fig. 4. In panel (a), when ω_I just lies below the vacuum band, the surface wave moves along the positive direction and is robust to any scattering process. When we increase ω_I a little bit so that it overlaps with the vacuum band, the surface wave is scattered into vacuum at defective points and source [panel (b)]. If ω_I overlaps with both vacuum and bulk bands, as well as the gapless surface state, the electromagnetic waves diffuse into the entire space while the right side has a stronger field intensity [panel (c)]. Finally, since the chirality of edge states is determined by sign$[\Im(\epsilon_{xy})]$, the surface wave indeed travels along the opposite direction when the gyromagnetic term is changed to an opposite sign in Fig. 4(d).

Here, we mainly concern the simulations with gyromagnetic terms while the chirality cases are studied in the Supplemental Material [30].

Discussions and conclusion.—We have considered a HMM with hyperbolicity on the permittivity tensor, which, however, is not necessary for the existence of chiral surface wave. For instance, a HMM with $\epsilon = I$ and $(\mu_x > 0, \mu_y > 0, \mu_z < 0)$ may also exhibit chiral surface waves under proper time-reversal (or inversion) symmetry breaking. Besides ϵ_{xy}, the gyromagnetic effects can also be generated by nondiagonal terms in μ. Indeed, a purely imaginary μ_{xy} induces chiral surface waves in a similar way, which, however, becomes topologically trivial (gapless) upon passing the critical point $\Im(\mu_{xy}) = \pm\sqrt{\mu_x \mu_y}$ [30].

For experimental considerations, the chiral effects exist in a range of natural materials [41] while the advances of metamaterials allow us to synthesize strong chiral media [42]. To achieve gyromagnetic effects, magnetic materials can be mixed during fabrication and one commonly used material is Yttrium-Iron-Garnet [20].

The topological band theory described here can be applied to various parameter regions and many interesting

effects, such as gain and loss [43], disorder, and bianisotropy terms with more general γ tensor, remain to be explored. The hyperbolic band dispersion of the topological HMMs opens a new avenue for studying negative refraction with topological edge states as well as topological lasing. In particular, the topological edge states in HMMs may be used to design a *topological-semimetal laser*. By tuning the structure of HMM and gyromagnetic or chiral field, the topological edge mode can be promoted to the lasing mode, rendering a highly efficient single-mode laser, which is robust to local disorders and defects. Note that although the bulk spectrum of HMMs could be complex, the topological edge spectrum is purely real. Thus it does not suffer from the inherent loss, which is the primary roadblock to the insertion of bulk HMMs into practical technologies. Because of the important and unique properties of HMMs like broad-band spontaneous emission enhancement (thus, the lasing threshold would be very small) and the ability to support propagations of large-momentum waves [2], the topological-semimetal laser may outperform recently emerged topological insulator laser using photonic crystals [44,45].

In conclusion, we developed a topological band description for the non-Hermitian continuous HMMs and found two types of non-Hermitian photonic triply degenerate points (classified by their topological charges) with different surface states. Our work should provide physical understanding of topological phases in HMMs and may inspire further theoretical and experimental investigations on the fundamental properties as well as practical applications of topological photonic continua.

We thank W. Gao for helpful discussions about COMSOL simulations. This work was supported by Air Force Office of Scientific Research (FA9550-16-1-0387), National Science Foundation (PHY-1505496), Army Research Office (W911NF-17-1-0128) and the UT Dallas Office of Research through the SPIRe Grant Program. Z. Li and Q. Gu acknowledge funding from the Welch Foundation (AT-1992-20190330) and UT Dallas faculty start-up funding.

*xiwang.luo@utdallas.edu
†chuanwei.zhang@utdallas.edu

[1] D. R. Smith and D. Schurig, Electromagnetic Wave Propagation in Media with Indefinite Permittivity and Permeability Tensors, Phys. Rev. Lett. **90**, 077405 (2003).
[2] A. Poddubny, I. Iorsh, P. Belov, and Y. Kivshar, Hyperbolic metamaterials, Nat. Photonics **7**, 948 (2013).
[3] Z. Jacob, L. V. Alekseyev, and E. Narimanov, Optical Hyperlens: Far-field imaging beyond the diffraction limit, Opt. Express **14**, 8247 (2006).
[4] Z. Liu, H. Lee, Y. Xiong, C. Sun, and X. Zhang, Far-field optical hyperlens magnifying sub-diffraction-limited objects, Science **315**, 1686 (2007).
[5] A. V. Kabashin, P. Evans, S. Pastkovsky, W. Hendren, G. A. Wurtz, R. Atkinson, R. Pollard, V. A. Podolskiy, and A. V. Zayats, Plasmonic nanorod metamaterials for biosensing, Nat. Mater. **8**, 867 (2009).
[6] M. Shoaei, M. K. Moravvej-Farshi, and L. Yousefi, All-optical switching of nonlinear hyperbolic metamaterials in visible and near-infrared regions, J. Opt. Soc. Am. B **32**, 2358 (2015).
[7] T. Galfsky, Z. Sun, C. R. Considine, C. T. Chou, W. C. Ko, Y. H. Lee, E. E. Narimanov, and V. M. Menon, Broadband enhancement of spontaneous emission in two-dimensional semiconductors using photonic hypercrystals, Nano Lett. **16**, 4940 (2016).
[8] D. Lu, J. J. Kan, E. E. Fullerton, and Z. Liu, Enhancing spontaneous emission rates of molecules using nanopatterned multilayer hyperbolic metamaterials, Nat. Nanotechnol. **9**, 48 (2014).
[9] L. Ferrari, J. S. T. Smalley, Y. Fainman, and Z. Liu, Hyperbolic metamaterials for dispersion-assisted directional light emission, Nanoscale **9**, 9034 (2017).
[10] R. Chandrasekar *et al.*, Lasing action with gold nanorod hyperbolic metamaterials, ACS Photonics **4**, 674 (2017).
[11] C. Liu, W. Gao, B. Yang, and S. Zhang, Disorder-Induced Topological State Transition in Photonic Metamaterials, Phys. Rev. Lett. **119**, 183901 (2017).
[12] W. Gao, M. Lawrence, B. Yang, F. Liu, F. Fang, B. Béri, J. Li, and S. Zhang, Topological Photonic Phase in Chiral Hyperbolic Metamaterials, Phys. Rev. Lett. **114**, 037402 (2015).
[13] R.-L. Chern and Y. Z. Yu, Chiral surface waves on hyperbolic-gyromagnetic metamaterials, Opt. Express **25**, 11801 (2017).
[14] Note that the term "continuous" here is defined in the context of long wave limit, where the period for the lattice structure to generate hyperbolic metamaterials is much shorter than the optical wavelength.
[15] T. Ozawa *et al.*, Topological photonics, Rev. Mod. Phys. **91**, 015006 (2019).
[16] L. Lu, J. D. Joannopoulos, and M. Soljacic, Topological photonics, Nat. Photonics **8**, 821 (2014).
[17] A. B. Khanikaev and G. Shvets, Two-dimensional topological photonics, Nat. Photonics **11**, 763 (2017).
[18] F. D. M. Haldane and S. Raghu, Possible Realization of Directional Optical Waveguides in Photonic Crystals with Broken Time-Reversal Symmetry, Phys. Rev. Lett. **100**, 013904 (2008).
[19] S. Raghu and F. D. M. Haldane, Analogs of quantum-Hall-effect edge states in photonic crystals, Phys. Rev. A **78**, 033834 (2008).
[20] Z. Wang, Y. Chong, J. D. Joannopoulos, and M. Soljacic, Observation of unidirectional backscattering-immune topological electromagnetic states, Nature (London) **461**, 772 (2009).
[21] A. Raman and S. Fan, Photonic Band Structure of Dispersive Metamaterials Formulated as a Hermitian Eigenvalue Problem, Phys. Rev. Lett. **104**, 087401 (2010).
[22] L. Lu, C. Fang, L. Fu, S. G. Johnson, J. D. Joannopoulos, and M. Soljačić, Symmetry-protected topological photonic crystal in three dimensions, Nat. Phys. **12**, 337 (2016).
[23] L. Wang, S.-K. Jian, and H. Yao, Topological photonic crystal with equifrequency Weyl points, Phys. Rev. A **93**, 061801 (2016).

[24] M. Xiao, Q. Lin, and S. Fan, Hyperbolic Weyl Point in Reciprocal Chiral Metamaterials, Phys. Rev. Lett. **117**, 057401 (2016).
[25] G. Siroki, P. A. Huidobro, and V. Giannini, Topological photonics: From crystals to particles, Phys. Rev. B **96**, 041408 (2017).
[26] B. Bahari, A. Ndao, F. Vallini, A. E. Amili, Y. Fainman, and B. Kanté, Nonreciprocal lasing in topological cavities of arbitrary geometries, Science **358**, 636 (2017).
[27] Z. Gao, Z. Yang, F. Gao, H. Xue, Y. Yang, J. Dong, and B. Zhang, Valley surface-wave photonic crystal and its bulk/edge transport, Phys. Rev. B **96**, 201402 (2017).
[28] M. Parto, S. Wittek, H. Hodaei, G. Harari, M. A. Bandres, J. Ren, M. C. Rechtsman, M. Segev, D. N. Christodoulides, and M. Khajavikhan, Edge-Mode Lasing in 1D Topological Active Arrays, Phys. Rev. Lett. **120**, 113901 (2018).
[29] M. G. Silveirinha, Chern invariants for continuous media, Phys. Rev. B **92**, 125153 (2015).
[30] See the Supplemental Material at http://link.aps.org/supplemental/10.1103/PhysRevLett.124.073603 for more details about the band structure, quantization of band Chern number, Berry curvature of TDPs, surface wave by chirality effects, topological phase transition of TDPs, and a counterexample for EFS theory.
[31] B. Bradlyn, J. Cano, Z. Wang, M. G. Vergniory, C. Felser, R. J. Cava, and B. A. Bernevig, Beyond Dirac and Weyl fermions: Unconventional quasiparticles in conventional crystals, Science **353**, aaf5037 (2016).
[32] B. Q. Lv *et al.*, Observation of three-component fermions in the topological semimetal molybdenum phosphide, Nature (London) **546**, 627 (2017).
[33] H. Hu, J. Hou, F. Zhang, and C. Zhang, Topological Triply Degenerate Points Induced by Spin-Tensor-Momentum Couplings, Phys. Rev. Lett. **120**, 240401 (2018).
[34] J. Lekner, Optical properties of isotropic chiral media, J. Opt. **5**, 417 (1996).
[35] A. P. Schnyder, S. Ryu, A. Furusaki, and A. W. W. Ludwig, Classification of topological insulators and superconductors in three spatial dimensions, Phys. Rev. B **78**, 195125 (2008).
[36] A. Kitaev, Periodic table for topological insulators, superconductors, AIP Conf. Proc. **1134**, 22 (2009).
[37] S. Ryu, A. P. Schnyder, A. Furusaki, and A. W. W. Ludwig, Topological insulators and superconductors: Tenfold way and dimensional hierarchy, New J. Phys. **12**, 065010 (2010).
[38] Z. Gong, Y. Ashida, K. Kawabata, K. Takasan, S. Higashikawa, and M. Ueda, Topological Phases of Non-Hermitian Systems, Phys. Rev. X **8**, 031079 (2018).
[39] H. Shen, B. Zhen, and L. Fu, Topological Band Theory for Non-Hermitian Hamiltonians, Phys. Rev. Lett. **120**, 146402 (2018).
[40] M. I. Dyakonov, New type of electromagnetic wave propagating at an interface, Sov. Phys. JETP **67**, 714 (1988).
[41] A. J. Viitanen, A. Sihvola, I. V. Lindell, and S. Tretyakov, *Electromagnetic Waves in Chiral and Bi-Isotropic Media* (Artech Print, Artech House, 1994).
[42] S. S. Oh and O. Hess, Chiral metamaterials: Enhancement and control of optical activity and circular dichroism, Nano Convergence **2**, 24 (2015).
[43] L. Feng, R. El-Ganainy, and L. Ge, Non-Hermitian photonics based on parity–time symmetry, Nat. Photonics **11**, 752 (2017).
[44] G. Harari, M. A. Bandres, Y. Lumer, M. C. Rechtsman, Y. D. Chong, M. Khajavikhan, D. N. Christodoulides, and M. Segev, Topological insulator laser: Theory, Science **359**, eaar4003 (2018).
[45] M. A. Bandres, S. Wittek, G. Harari, M. Parto, J. Ren, M. Segev, D. N. Christodoulides, and M. Khajavikhan, Topological insulator laser: Experiment, Science **359**, eaar4005 (2018).